DOI: 10.1002/((please add manuscript number))
Article type: Communication

3D-printed Structural Pseudocapacitors

Xinhua Liu[1], Rhodri Jervis[2], Robert C. Maher[3], Ignacio J. Villar-Garcia[4], Max Naylor-Marlow[5], Paul R. Shearing[2], Mengzheng Ouyang,[6] Lesley Cohen[3], Nigel P. Brandon[6] and Billy Wu[1]**

[*] Dr. X. Liu, Dr. Billy Wu
Dyson School of Design Engineering, Imperial College London, UK
E-mail: x.liu15@imperial.ac.uk, billy.wu@imperial.ac.uk

Dr. R. Jervis, Prof. Dr. P. R. Shearing
Department of Chemical Engineering, University College London, UK

Dr. R. C. Maher, Prof. Dr. L. Cohen
Department of Physics, Imperial College London, UK

Dr. I. J. Villar-Garcia
Department of Materials, Imperial College London, UK

M. Naylor-Marlow
Department of Mechanical Engineering, Imperial College London, UK

M. Ouyang, Prof. Dr. N. P. Brandon
Department of Earth Science and Engineering, Imperial College London, UK

Keywords: 3D printing; Pseudocapacitor; Co-electro-deposition; X-ray tomography

Recent technological trends toward electronic devices requiring reduced weight, opens the possibility for structural energy storage devices which have high energy and power densities whilst offering mechanical load carrying capability. Pseudosupercapacitors are a particularly attractive class of energy storage devices because they combine the advantages of fast surface charge storage and bulk intercalation processes to enable high power and energy density respectively.[1-3] However, successful translation of laboratory findings towards scalable industrial applications require the identification of low cost electrode materials with high areal capacitance.[4] Manganese oxides have attracted broad research interest because of their low cost, abundance, and high theoretical specific capacitance (1,370 F/g).[5,6] However, they suffer from poor electronic conductivity and limited cycling stability. To address this issue, manganese oxides have been assembled with other conductive matrixes, such as graphene,[7,8] carbon nanotubes,[9] and conducting polymers,[10] to form a variety of composite materials which are suitable candidates as pseudocapacitor electrodes. Among them, the binderless composites of MnO_2 with conducting polymers are among the most promising materials which afford improved energy densities compared to conventional carbon based supercapacitors. Furthermore, conducting polymers such as polypyrrole, polyaniline and poly[3,4-ethylenedioxythiophene] (PEDOT) not only act as binders but do themselves exhibit pseudocapacitive behaviour through redox processes associated with the π-conjugated polymer chains. During oxidation/reduction, ions from the electrolyte are transferred onto the backbone of the polymer. This doping/undoping is a bulk process which enables a high specific capacitance; however it can also lead to large volumetric expansion resulting in fracture of the electrode.[11]

Current pseudocapacitor research is mainly focused on the preparation of nanostructured electroactive materials,[12-14] however current collector morphology is also a critical factor in achieving improved electrochemical performances. Liu et al., for instance, showed that fine control of the three-dimensional (3D) electrode/current collector geometry can significantly improve ion diffusion in their all-in-one nanopore battery array which uses a series of single nanotubes as the current collector to host electroactive materials.[15] Such an array template could present an alternative to interdigitated electrode structures with 3D spatial heterogeneity. However, these conventional templates cannot meet the demands for structural energy storage applications because of their limited mechanical strength.

3D metal printing (direct metal laser sintering) is a key additive manufacturing technology, enabling increased design flexibility and rapid processing of complex forms. [16,17] Thus, this technology has been applied in numerous applications, such as automotive, aerospace, defence, energy devices, and other engineering industries.[18-21] The potential of the technology has still yet to be fully realised, with components frequently being designed with only a single criteria in-mind (e.g. structural, thermal or geometric), and thus not fully utilising the design freedom of 3D printing. Inspired by this, we present the use of 3D metal printing to create porous scaffolds with high strength and surface area, which we subsequently functionalise with electroactive material to realise structural energy storage devices. This methodology can therefore have a broad impact on other electrochemical devices, for instance, optimised 3D printed metal foams can benefit the performance of redox flow cells, improving the electrochemical surface area and controlling the flow of electrolyte.[22,23] However, current applications of 3D printing in electrochemical applications are still embryonic. Furthermore, the majority of academic works in 3D metal printing have focused on obtaining fully dense structures. However, many electrochemical devices require porosity, and the potential of 3D printing to create controlled porosity for this application is highly timely and can open new fields of research.

Here we demonstrate that metal scaffolds with controllable porosity can be obtained by 3D printing through control of laser power and scan speed, creating structures that can be optimised for the mass transport of charge carriers and increase electroactive surface area. These efforts offer a route to reducing ohmic, charge transfer and mass transport resistances and thereby enable the next generation of pseudocapacitors. In this study, a co-electro-deposition method was employed to produce uniform electroactive MnO_2, Mn_2O_3 and PEDOT:PSS (MnO_x-PEDOT:PSS) films on printed stainless steel scaffolds. The advantage of this structured substrate approach is that it improves device lifetime, by limiting the effects of the volumetric expansion experience by the pseudocapacitive material.

To understand the interaction of the active material with the scaffold structures we employ X-ray tomography which has enabled researchers to obtain unprecedented insight into microstructural evolution of electrodes in Li-ion batteries and other electrochemical devices.[24-26] Here we present the first multi-scale high-resolution micro/nano X-ray tomography study of pseudocapacitor materials, and demonstrate the power of the technique to quantify the distribution and morphology of the deposited material before and after charge cycling. The development of additive manufacturing in combination with advanced characterisation techniques thus demonstrates the advantages of this methodology for the development of next generation pseudocapacitors with increased lifetime and capacitance.

This work is based on the preparation of MnO_x-PEDOT:PSS films on 3D printed stainless steel 316L (hereafter referred to as stainless steel) scaffolds for pseudocapacitor applications. The printed stainless steel scaffolds were designed to be square-shaped with a porous upper layer (5 × 5 mm, thickness=100 μm) and a fully dense supporting layer (5 × 5 mm, thickness=200 μm). Porosity can be introduced by varying the laser power and scan speed of the upper layer. As illustrated in **Figure 1**a, a laser power of 90 W and scan speed of 1500 mm/s (90-1500 is used here to represent the laser power (W) and scan speed (mm/s) respectively) is optimized to print a fully dense structure. In this study, the laser parameters are selected as 45-600, 45-900, 45-1200, and 45-1500 to obtain various plates (Figure 1b) and plate-arrays (Figure 1c) with controllable porosity and surface area, through partial sintering of the stainless steel powder.

Co-electro-deposition can produce a uniform MnO_x-PEDOT:PSS nanostructured film on the printed scaffolds. The MnO_x-PEDOT:PSS can be deposited on both the dense (Figures 1d and 1g) and porous (Figures 1e and 1h) plates. The porous scaffold with higher specific surface area can host an increased quantity of active material (Figure 1k), while the fully dense support achieves a lower mass loading (Figure 1j) because of its reduced surface area. Therefore, the porous plate can be further refined to the plate-array design, which can achieve larger surface area and mass loading (Figures 1f and 1i). The film thickness required to achieve equivalent mass loading is a critical factor due to the limited electrical conductivity of the MnO_x phase, and optimisation of this layer is important to achieve high material utilisation.

The MnO_x-PEDOT:PSS composite electrode was synthesized by co-electro-deposition which consists of the simultaneous electrophorectic deposition (EPD) of colloidal PEDOT:PSS and the anodic electrochemical deposition of MnO_x. In a typical deposition process, co-electro-deposition was performed in an aqueous solution containing 50 ml (0.1 M) of manganese (II) acetyllacetonate ($Mn(AC)_2$) and 0.2 ml PEDOT:PSS aqueous solution (4 wt%) applying a DC voltage of 10.0 V. The MnO_x-PEDOT:PSS composite electrodes were analysed by X-ray photoelectron spectroscopy (XPS) to investigate the oxidation state of Mn in the composite electrode. The Mn 2p spectrum (shown in **Figure 2**g) exhibits binding energies and shapes characteristic of Mn_2O_3,25-27 which indicates that the majority of the MnO_x is Mn_2O_3. The O 1s spectrum (Figure 2h) exhibits two major peaks at the characteristic binding energies of bulk Mn–O–Mn (529.9 eV) and terminal Mn-OH (531.6 eV) groups in MnO_x compounds.[27-29] Moreover, the separation in energy (ΔE_b) of the multiplet splitting in the Mn 3s spectrum (Figure S1) is 5.5 eV which is the characteristic separation for Mn_2O_3. Raman spectra of MnO_x and MnO_x-PEDOT:PSS are shown in Figure 2i. Compared to the Raman spectra (Figure S2) of the stainless steel, PEDOT:PSS, and $Mn(AC)_2$, the peak between 640-645 cm^{-1} demonstrates that mixed MnO_2 (645 cm^{-1}) and Mn_2O_3 (641 cm^{-1}) exist simultaneously.[30-32] The most obvious difference that was observed is the peak around 1,450 cm^{-1} which can be attributed to PEDOT:PSS. Moreover, the shoulder at 532.8 eV in the O 1s spectrum (Figure 2g) is identified as the characteristic binding energy of the C-O-C moieties as found in the PEDOT structure. The S 2p spectra in Figure S3 also exhibits PEDOT:PSS characteristic peaks with a 4:6 approx. ratio.[33] These sulfur atoms are present in an approximately 3.4 relative atomic % (see in table S1) in the MnO_x-PEDOT:PSS composites**.** Therefore, driven by the electrostatic field, the PEDOT:PSS (with a Zeta potential of -26.69 mV at pH=7) can be tightly attached to the MnO_x nanoparticles in the anode and thus act as binder to form a uniform composite film.

Figure 2a shows a scanning electron microscopy (SEM) image of a fully dense plate printed with a laser power/speed of 90-1500. Here it is evident that the surface area and porosity are limited, however, by reducing the laser energy density, the surface area and porosity of the scaffold increases substantially due to the partial sintering of the metal powder as shown in Figure S5. According to our previous work, [34] increasing printing scan speed resulted in an increase in porosity when laser power was fixed as a constant value. A higher porosity of 29.23% was observed using a scan speed of 1500 mm/s compared to the porosity of 9.57% at 600 mm/s, both with a fixed laser power of 45 W.

Inspired by the various academic works involving interdigitated batteries, the design was further refined to incorporate aligned arrays onto the plates to further improve the surface area. Figure 2b shows one such plate-array scaffold with a laser power and scan speed of 45-1200, where the arrays are 5 mm in length, 200 μm in width, and 200 μm in height. Other plate-array scaffolds with different laser parameters are shown in Figure S8. Photographs of the arrangement of the scaffolds in the direct metal laser sintering machine are shown in Figure S4. After the co-electro-deposition of MnO_x-PEDOT:PSS on the various scaffolds it is evident that a film of active material is present (Figure 2c, 2d, S6 and S9), whereby the mass loading is a function of the scaffold surface area and the deposition time (Figure S7 and S10). Higher magnification SEM images reveals multi-scale features of the deposition. In Figure 2e, a reasonably dense but mossy film is observed over the partially sintered metal particles. Figure 2f then shows the sub-surface morphology of the active material observed through a crack in the electrode. Here 2 distinct nano-structures can be observed; a cactus-like MnO_x structure evident through the increased charging of that region owing to its lower electronic conductivity, and spherical nano-particles characteristic of the colloidal PEDOT:PSS particles. The two structures are shown to be well mixed as originally designed, so that the conducting polymer can enable higher utilisation of the MnO_x through improvements in its limited electronic conductivity. Although the printed scaffold with laser parameters of 45-1500 achieved the highest porosity, the plate-array exhibited poor mechanical strength. In view of the high porosity and good mechanical integrity, the plate and array printed at 45-1200 was selected as the ideal choice. The mass loading of the activated material with this substrate can reach as high as 9.2 mg/cm^2 within a 25 minute deposition time.

The electrochemical properties of the as-prepared samples were measured. It has been proven that PEDOT:PSS can act as effective binder to improve both the conductivity and capacitance of MnO_x by accelerating the charge transfer process related to the Mn^{2+} ions. The specific capacitances (Csp) with respect to the mass loading of MnO_x-PEDOT:PSS on printed scaffolds at various scan rate ranging from 1 to 100 mV/s are plotted in Figure S11. For the dense plate, a high specific capacitance of 609 F g^{-1} can be achieved at 1 mV/s with a low mass loading of 0.40 mg cm^{-2}. However, this high specific capacitances value can only be observed when a thin active material layer is used at low scan rate. In order to achieve practical devices, high mass loadings, scan rate performance and areal capacitance are of critical importance. By increasing the deposition time from 5 min to 25 min, the mass loading of MnO_x-PEDOT:PSS increases from 0.40 to 3.10 mg cm^{-2} for the dense plates, however this is coupled with a decrease in specific capacitance (Figure S11a). However, as the mass loading increases, the areal capacitances of the printed dense electrodes is improved from 0.24 F cm^{-2} to 0.43 F cm^{-2} (**Figure 3**a) which is still lower than reported values of 0.5 F cm^{-2}.[35-37] The limited capacitance values can be attributed to the low surface area of the printed dense plate and thick active material films.

Moving to the porous plates, the specific and areal capacitances are shown in Figures S11 and S12 respectively. Here it is evident that at lower laser energy densities, the performance, both in terms of specific and areal capacitance is improved due to thinner active material films for equivalent mass loading. Focusing on the areal capacitance as the critical figure of merit, the plate-array scaffold built with a laser power and speed of 45-1200 and 25 min deposition shows excellent CV performances and the highest areal capacitance of 1.50 F cm^{-2} at a mass loading of 9.2 mg cm^{-2} (Figures S13 and S14). The electrochemical performance increase from going from dense plate to porous plate to porous plate-array scaffolds is highlighted in Figure 3c which shows the cyclic voltammetry (CV) curves of the three structures with an equivalent deposition time of 25 minutes under a scan rate of 25 mV/s. Direct performance comparison of the various mass loadings on the different scaffolds is then shown in Figure 3d. With an equivalent mass loading of MnO_x-PEDOT:PSS, the porous plate-array scaffold (45-1200) electrode possess the highest areal capacitances.

This approach also shows an effective and controllable process to obtain time-dependent thicker active materials on metal scaffolds (over 9.2 mg cm^{-2} within 25 minutes). As shown in Figure S15 and S16, the areal capacitance calculated from charge/discharge method increases accordingly with the mass loading applying various printed scaffolds which is inline with the values obtained from CV curves. The specific capacitance is much higher than most metal scaffold related supercapacitors.[38-39] A high areal capacitance value of 1.52 F cm^{-2} at the current density of 1 mA cm^{-2} (Figure S16d) of the plate and array scaffold with a laser power and speed of 45-1200 and 25 min deposition has been achieved, which is much higher than most previously reported areal capacitances of supercapacitors.[40-42]

To explore the mechanism for the improved performance, charge transfer resistance (R_{ct}) was measured by electrochemical impedance spectroscopy. As presented in Figure 3e, the R_{ct} of the electrodes with the more porous scaffold is lower than that of dense substrate with an equivalent mass loading. As illustrated in Figures 3f and 3g, the porous structure can enhance the specific capacitance of the device in two distinct ways. With a thicker layer of MnO_x-PEDOT:PSS on the surface of the dense scaffolds, the diffusion resistance of ions to deeper pores, and the electrical conductivity of the electrode material starts becoming a critical factor, limiting performance and decreasing material utilisation. In the case of the porous scaffolds, the active material can form thinner layers for the equivalent mass loading because of the improved surface area. This improves the accessible surface area and improves electronic conductivity through a combination a thinner film and the porous stainless steel which can act as suitable conducting pathways to improve the efficiency during high current density charging and discharging process.

The printed porous structures show great advantages with respect to improving the reaction efficiency compared to dense substrates with the same mass loading. Furthermore, the cycling behaviour of the dense (90-1500) and porous plate-array scaffold (45-1200) electrodes were investigated (**Figure 4**b). With the same deposition time of 5 min, the porous scaffold can host more active material and thus exhibits a higher areal capacitance than the dense electrode. More importantly, the porous plate-array scaffold shows better cycling performance than the dense plate electrode (by approximately 3 times). As can be seen from Figures 4c and 4d, after 500 cycles, there are many cracks (magnified SEM image in Figure 4a) and most of the active material delaminates from the dense plate. In contrast, the porous scaffold can retain most of the active material after 1600 cycles (Figures 4e and 4f). Therefore, the porous scaffold reduces the delamination of active materials originating from the volume expansion in the charging-discharging process through mechanical confinement within the rigid pores and geometry of the deposition.

To investigate this further, X-ray computed tomography (XCT) was employed to analyse the 3D microstructure of the electrodes and was used as an approach to provide new insight into the cycling mechanisms. **Figure 5**a shows the X-ray reconstruction of the pre-cycled porous plate and array sample with higher mass loading (6 mg cm^{-2}). Figure 5b then shows an orthogonal slice through the 3D reconstruction, with the stainless steel and deposition phases as grey and purple respectively. The digital analysis of the reconstruction indicates that partial sintering of the scaffold structures and incorporation of the arrays results in a substrate surface area enhancement of 8 fold and a 13 fold improvement in the active material surface area relative to the planar area. After 1,600 cycles, the porous scaffold was shown to retain most of the deposited electroactive material. Comparing the surface area ratio of the active material to the stainless steel before and after 1,600 cycles, the XCT measurements suggest a 20% reduction in available surface area due to loss of active material.

Although the Zeiss Xradia Versa 520 can give a sufficiently wide field of view to achieve a full sample scan thereby providing useful surface information, the resolution and contrast was not optimized to describe detailed microstructural features of the co-electro-deposited material. Therefore, subsequent higher resolution scans were conducted with a much smaller field of 65 × 65 μm. Figures 5c and 5d show the 3D reconstructions of the stainless steel and deposition phases using the same colour coding, indicating the close connection of the two phases. These high resolution XCT measurements indicate an electrode morphology supported by the SEM images (Figure 4a), whereby there is a dense lamella like structure at the surface and a highly porous sub-surface structure, with cracks propagating through the electrode at various points. Upon cycling, the volumetric changes in the electrode cause additional cracking of the electrodes which enables the accessibility of more electrode surface area (and thus increased performance), as the top layer is denser than the inner layers (Figure 5e). This supports the observed increase in areal capacitance seen in Figure 4b on the initial cycles. The porous scaffold therefore aids device lifetime in two proposed ways. Pore confinement prevents electrode delamination from the current collecting scaffold which would otherwise increase series resistance. In addition, pore confinement minimises the electrode strain caused by the volumetric expansion associated with the adsorption/desorption of ions as well as the intercalation/deintercalation processes, thus retaining more active material which is evident from the SEM images.

Our findings therefore underline a novel approach of combining 3D printed stainless steel scaffolds with a co-electro-deposition of MnO_x-PEDOT:PSS to achieve a pseudocapacitor with high areal capacitance, lower resistance and longer cycling performance. The volume expansion during the charging-discharging process can be reduced within the pores of the scaffold, thus the porous structure can avoid the delamination of active materials and benefit the cycling behaviour. New insights have therefore been presented for the development of 3D printed pseudocapacitors with potential load carrying capabilities, and highlights the opportunity develop other 3D printed energy storage devices.

Experimental Section

3D printing process: Printed scaffolds were fabricated by employing a Concept Laser mLab and a direct metal laser sintering system (with a 100 W fibre laser system with a 35 µm focal diameter), under a nitrogen atmosphere. Stainless steel 316L powder (CL 20ES) with an average particle diameter of 26.9 µm (d50) was used. The geometric files were prepared using Solidworks which were converted into .stl file format for input into the software Magics which generated the laser slice data.

Characterizations: The high resolution X-ray scans were performed on a Zeiss Xradia Ultra 810, and the full body scans were obtained on a Zeiss Xradia Versa 520. The further image processing and surface area analysis was done by using Avizo. The morphology images of the printed scaffolds with/without deposition were characterized by the scanning electron microscope (JSM 5610 LV SEM, JEOL, Japan) at the acceleration voltage of 15 kV. The images with higher magnification were obtained by a ZEISS Auriga (Carl Zeiss Microscopy, Germany) at the acceleration voltage of 5 kV. X-ray photoelectron spectroscopy (XPS) measurements (Thermo K-Alpha) were performed to analyse the surface species and their chemical states. PALS Zeta Potential Analyser version 3.48 (Brookhaven Instruments) was used to collect the Zeta potential of PEDOT:PSS. Raman characterization was performed using a Renishaw RM-2000 confocal microscope CCD system with a 514 nm laser at low power focused using the ×50 short working distance objective.

The electrochemical properties of the MnOx-PEDOT:PSS deposited electrodes were investigated on a Metrohm Autolab PGSTA302N potentiostat-galvanostat (The Netherlands) by a typical three-electrode conguration in LiTFSI aqueous electrolyte (0.25 M). The as-prepared samples were the working electrodes with an electrode area of 0.25 cm^2, and the platinum plate electrode (area of 1 cm^2) and a saturated calomel electrode (SCE) were used as the counter and reference electrodes, respectively.

Supporting Information

Supporting Information is available online from the Wiley Online Library or from the author.

Acknowledgements

This work is supported by the EPSRC capital grant for Energy storage for low carbon grids (EP/J0211991/1) and EPSRC capital grant for medical robotics (EP/J021199/1). The authors would like to thank M. Chakrabarti and D. Nir for the zeta potential measurements, F. Tariq for assistance with the XCT measurements and M. Biton for assistance with SEM measurements.

Received: ((will be filled in by the editorial staff))
Revised: ((will be filled in by the editorial staff))
Published online: ((will be filled in by the editorial staff))

[1] H. Li, M. Yu, F. Wang, P. Liu, Y. Liang, J. Xiao, C. Wang, Y. Tong, G. Yang, *Nat. Commun.* **2013**, *4*, 1894.

[2] D. Z. W. Tan, H. Cheng, S. T. Nguyen, H. M. Duong, *Mater. Technol* **2014**, *29*, A107.

[3] P. Simon, Y. Gogotsi, *Nat. Mater.* **2008**, *7*, 845.

[4] P. Yang, Y. Ding, Z. Lin, Z. Chen, Y. Li, P. Qiang, M. Ebrahimi, W. Mai, C. P. Wong, Z. L. Wang, *Nano Lett.* **2014**, *14*, 731.

[5] X. Lu, M. Yu, G. Wang, T. Zhai, S. Xie, Y. Ling, Y. Tong, Y. Li, *Adv. Mater.* **2013**, *25*, 267.

[6] M. Toupin, T. Brousse, D. Bélanger, *Chem. Mater.* **2004**, *16*, 3184.

[7] G. Yu, L. Hu, N. Liu, H. Wang, M. Vosgueritchian, Y. Yang, Y. Cui, Z. Bao, *Nano Lett.* **2011**, *11*, 4438.

[8] L. Peng, X. Peng, B. Liu, C. Wu, Y. Xie, G. Yu, *Nano Lett.* **2013**, *13*, 2151.

[9] L. Hu, W. Chen, X. Xie, N. Liu, Y. Yang, H. Wu, Y. Yao, M. Pasta, H. N. Alshareef, Y. Cui, *ACS Nano* **2011**, *5*, 8904.

[10] G. Han, Y. Liu, L. Zhang, E. Kan, S. Zhang, J. Tang, W. Tang, *Sci. Rep.* **2014**, *4*, 4824 doi:10.1038/srep04824.

[11] R. Österbacka, C. P. An, X. Jiang, Z. V. Vardeny, *Science* **2000**, *287*, 839.

[12] J. Xiao, L. Wan, S. Yang, F. Xiao, S. Wang, *Nano Lett.* **2014**, *14,* 831.

[13] R. Mukkabla, M. Deepa, A. K. Srivastava, *Electrochimi Acta* **2015**, *164*, 171.

[14] Q. Yang, Z. Lu, T. Li, X. Sun, J. Liu, *Nano Energy* **2014**, *7*, 170.

[15] C. Liu, E. I. Gillette, X. Chen, A. J. Pearse, A. C. Kozen, M. A. Schroeder, K. E. Gregorczyk, S. B. Lee, G. W. Rubloff, *Nat. Nanotechnol.* **2014**, *9*, 1031.

[16] A. Ambrosi, J. G. S. Moo, M. Pumera, *Adv. Funct. Mater.,* **2016,** *26,* 698.

[17] A. Ambrosi, M. Pumera, *Chem. Soc. Rev.*, **2016,** *45*, 2740.

[18] C. Zhao, C. Wang, R. Gorkin, S. Beirne, K. Shu, G. G. Wallace, *Electrochem Commun* **2014**, *41*, 20.

[19] A. S. Haselhuhn, E. J. Gooding, A. G. Glover, G. C. Anzalone, B. Wijnen, P. G. Sanders, J. M. Pearce, *3D Printing and Additive Manufacturing* **2014**, *1*, 204.

[20] T. J. Horn, O. L. Harrysson, *Science progress* **2012**, *95*, 255.

[21] T. B. Kim, S. Yue, Z. Zhang, E. Jones, J. R. Jones, P. D. Lee, *J. Mater Process Tech* **2014**, *214*, 2706.

[22] L. Arenas, F. Walsh, C. P. de León, *ECS J. Solid State Sc* **2015**, *4*, P3080.

[23] G. Chisholm, P. J. Kitson, N. D. Kirkaldy, L. G. Bloor, L. Cronin, *Energ. Environ. Sci.* **2014**, *7*, 3026.

[24] D. S. Eastwood, V. Yufit, J. Gelb, A. Gu, R. S. Bradley, S. J. Harris, D. J. Brett, N. P. Brandon, P. D. Lee, P. J. Withers, *Adv. Energy. Mater.* **2014**, *4*, DOI: 10.1002/aenm.201300506.

[25] D. S. Eastwood, P. M. Bayley, H. J. Chang, O. O. Taiwo, J. Vila-Comamala, D. J. Brett, C. Rau, P. J. Withers, P. R. Shearing, C. P. Grey, *Chem. Commun.* **2015**, *51*, 266.

[26] D. P. Finegan, M. Scheel, J. B. Robinson, B. Tjaden, I. Hunt, T. J. Mason, J. Millichamp, M. Di Michiel, G. J. Offer, G. Hinds, *Nat. Commun.* **2015**, *6*, 6924, doi:10.1038/ncomms7924.

[27] G. O. Park, J. K. Shon, Y. H. Kim, J. M. Kim, *J. Nanosci Nanotechno* **2015**, *15*, 2441.

[28] M. Fujiwara, T. Matsushita, S. Ikeda, *J Electron Spectrosc* **1995**, *74*, 201.

[29] Z. Su, C. Yang, C. Xu, H. Wu, Z. Zhang, T. Liu, C. Zhang, Q. Yang, B. Li, F. Kang, *J. Mater. Chem. A* **2013**, *1*, 12432.

[30] D. Chen, D. Ding, X. Li, G. H. Waller, X. Xiong, M. A. El-Sayed, M. Liu, *Chem. Mater.* **2015**, *27*, 6608.

[31] R. Craciun, N. Dulamita, *Catal. Lett.* **1997**, *46*, 229.

[32] Z. Chen, S. Tan, S. Zhang, J. Wang, S. Jin, Y. Zhang, H. Sekine, *Jpn J. Appl Phys* **2000**, *39*, 6293.

[33] J. Zhou, D. H. Anjum, G. Lubineau, E. Q. Li, S. T. Thoroddsen, *Macromolecules* **2015**, *48*, 5688.

[34] K. A. Ibrahim, B. Wu and N. P. Brandon, *Materials & Design*, **2016,** *106,* 51.

[35] L. Hu, M. Pasta, F. L. Mantia, L. Cui, S. Jeong, H. D. Deshazer, J. W. Choi, S. M. Han, Y. Cui, *Nano Lett.* **2010**, *10*, 708.

[36] L. Bonnefoi, P. Simon, J. Fauvarque, C. Sarrazin, J. Sarrau, A. Dugast, *J power sources* **1999**, *80*, 149.

[37] D. N. Futaba, K. Hata, T. Yamada, T. Hiraoka, Y. Hayamizu, Y. Kakudate, O. Tanaike, H. Hatori, M. Yumura, S. Iijima, *Nat. Mater.* **2006**, *5*, 987.

[38] P. Tang, L. Han and L. Zhang, *ACS Appl. Mater. Inter,* **2014,** *6,* 10506.

[39] R. Liu, J. Duay, S. B. Lee, *ACS Nano,* **2010,** *4,* 4299.

[40] Y. He, W. Chen, X. Li, Z. Zhang, J. Fu, C. Zhao, E. Xie, *ACS Nano,* **2013,** *7,* 174.

[41] A. Sumboja, C. Y. Foo, X. Wang and P. S. Lee, *Adv. Mater.*, **2013,** *25,* 2809.

[42] A. E. Fischer, K. A. Pettigrew, D. R. Rolison, R. M. Stroud and J. W. Long, *Nano Lett.*, **2007,** *7,* 281.

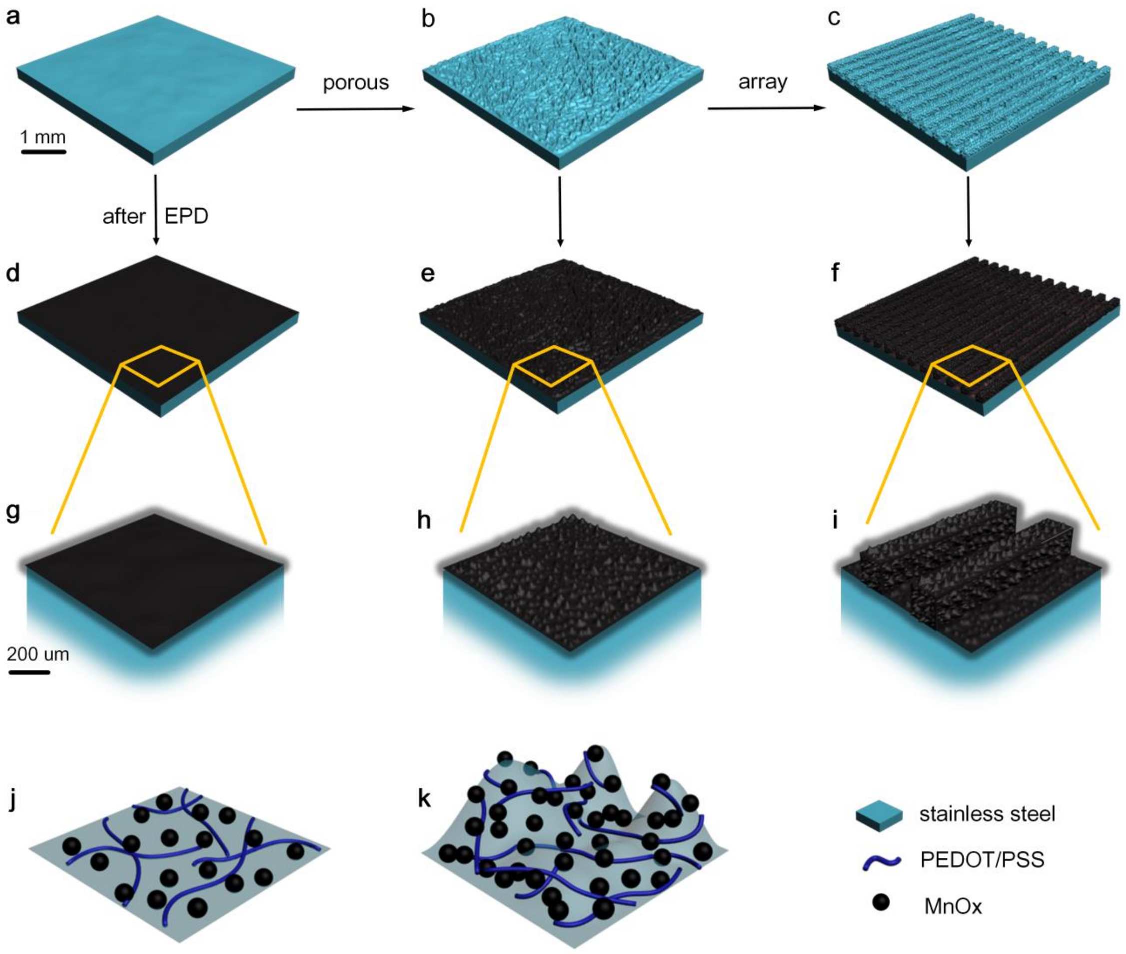

Figure 1. Schematic of 3D-printed stainless steel scaffolds and electrodeposited MnO_x-PEDOT:PSS. 3D-printed stainless steel scaffolds: (a) standard dense plate, (b) porous plate, and (c) porous plate and array. The obtained scaffolds with deposition of MnO_x-PEDOT:PSS (d-f) and at higher magnification (g-i). The one-step co-electro-deposition of MnO_x-PEDOT:PSS on dense stainless steel plate (j) and porous scaffold (k)

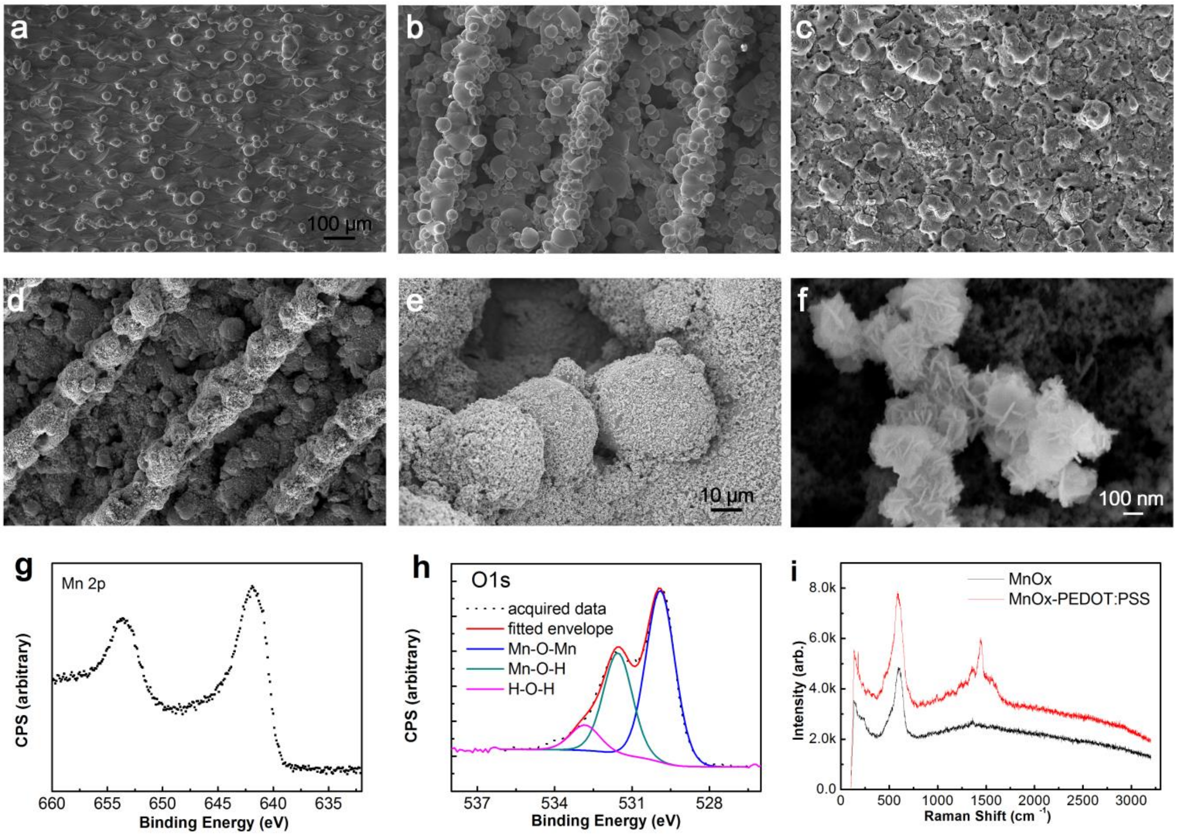

Figure 2. Characterisations of as prepared samples. Selected SEM images of the 3D-printed stainless steel scaffolds with different speed and laser power: (a) fully dense plate under 90-1500 and (b) porous plate and array under 45-1200. SEM images of the deposition of MnO_x-PEDOT:PSS on (c) fully dense plate under 90-1500 and (d) porous plate and array under 45-1200. The black scale bar represents 100 µm and is applied to all the above images. The SEM images of the composite deposition at low (e) and high (f) magnification. (g) Mn 2p and (h) O 1s high resolution XPS spectrum of the MnO_x-PEDOT:PSS nanocomposite deposition. i) Raman spectra of MnO_x and MnO_x-PEDOT:PSS nanocomposites.

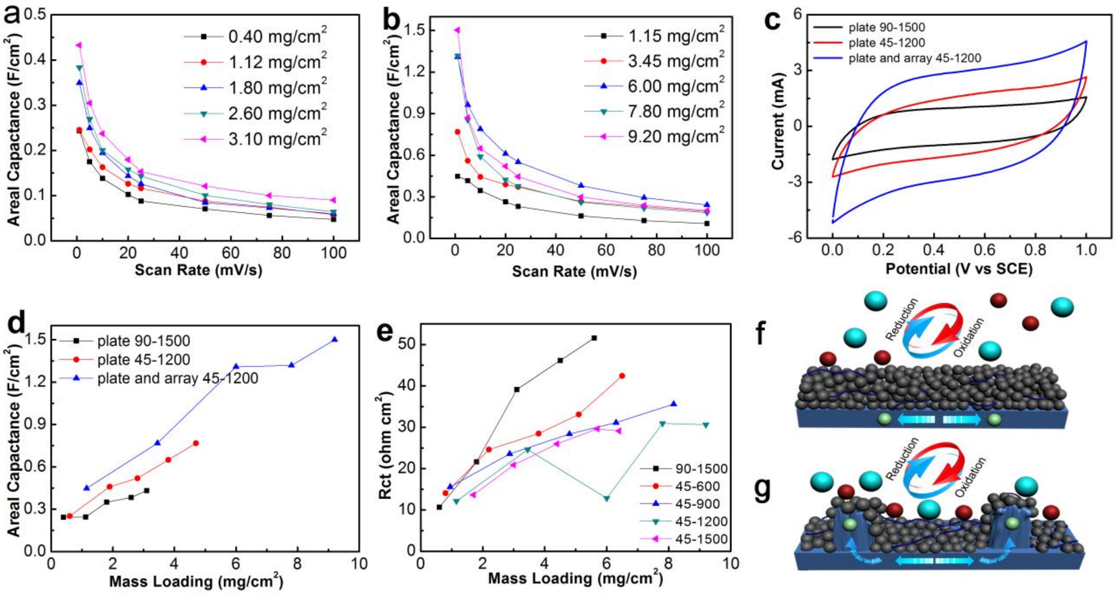

Figure 3. Electrochemical performances of as prepared samples. (a) Areal capacitance vs. scan rate for the MnO_x-PEDOT:PSS-dense electrode (90-1500) with different mass loadings. (b) Areal capacitance vs. scan rate for the MnO_x-PEDOT:PSS-porous plate and array electrode (45-1200) with different mass loadings. (c) CV curves of various plate/plate and array with 25 min deposition of MnO_x-PEDOT:PSS at 25 mV/s. (d) Areal capacitance vs. mass loading for the MnO_x-PEDOT:PSS based electrodes with different printing parameters. (e) R_{ct} vs. mass loading for the MnO_x-PEDOT:PSS based plate & array electrodes with different printing parameters. Schematic illustration showing the limitation of the dense plate (f) and the advantage of the porous structure (g).

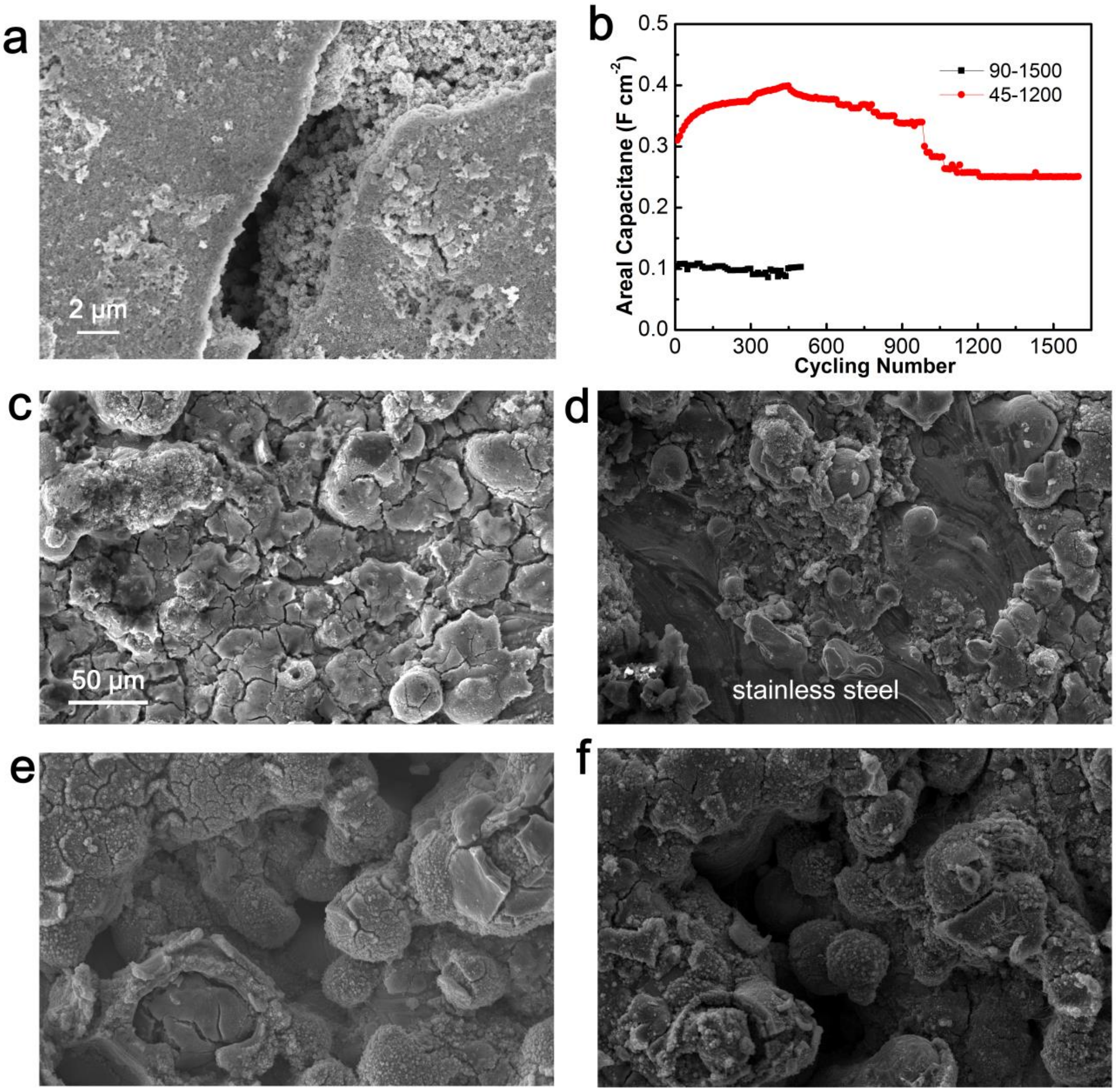

Figure 4. Proposed failure modes for electrodes with dense and porous structures. (a) SEM image of the MnO_x-PEDOT:PSS crack around stainless steel. (b) Cycling tests of the dense plate (90-1500) and porous plate and array (45-1200) with 5 min deposition. SEM images of the planar electrode before (c) and after (d) the cycling test. SEM images of the porous electrode before (e) and after (f) the cycling test.

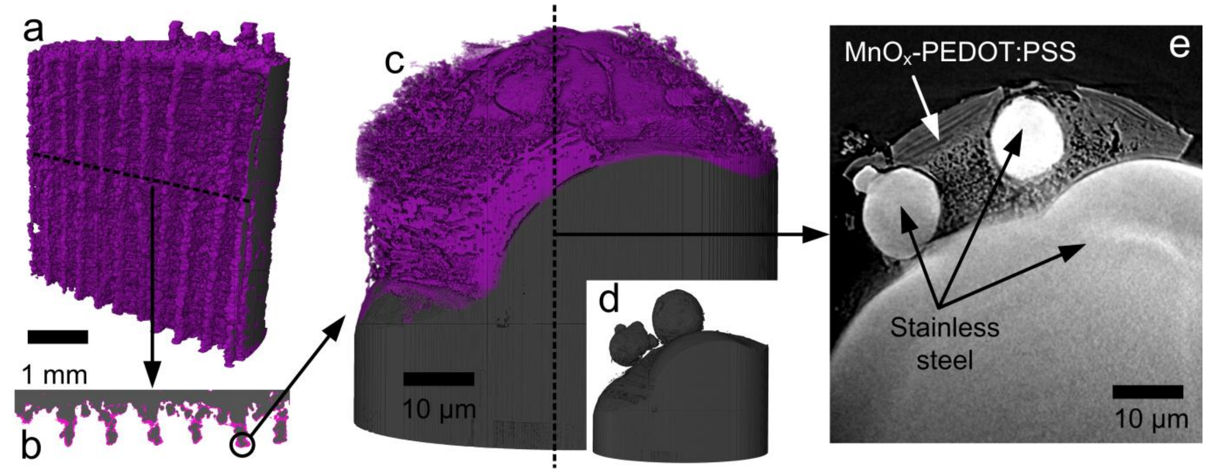

Figure 5. Proposed failure modes for porous plate & array electrode. X-ray tomography reconstruction of the plate-array scaffold with 15 min MnO$_x$-PEDOT:PSS deposition: (a) fresh full body scan and (b) a orthogonal slice with colour coding indicating the electroactive material and stainless steel phases. (c) high resolution XCT reconstruction of stainless steel and MnOx-PEDOT:PSS with (d) inset showing only the stainless steel phase. (e) Orthogonal slice of the high resolution XCT reconstruction showing the electrode morphology, cracks and current collector bonding.

The table of contents entry

Here we demonstrate the use of direct metal laser sintering to create 3D hierarchical porous metallic scaffolds which are then functionalised with a co-electro-deposition of MnO_2, Mn_2O_3 and doped conducting polymer. This approach of functionalising metal 3D printed scaffolds thus opens new possibilities for structural energy storage devices with enhanced performance and lifetime characteristics.

Keyword
3D printing; Pseudocapacitor; Co-electro-deposition; X-ray tomography

X. Liu, R. Jervis, R. C. Maher, I. J. Villar-Garcia, M. Naylor-Marlow, P. R. Shearing, M. Ouyang, L. Cohen, N. P. Brandon and B. Wu

3D-printed Structural Pseudocapacitors

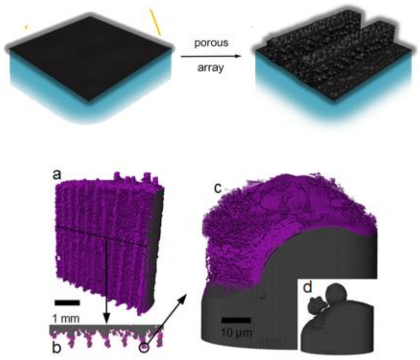

((Supporting Information can be included here using this template))

Supporting Information

3D-printed structural pseudocapacitors

Xinhua Liu, Rhodri Jervis, Robert C. Maher, Ignacio J. Villar-Garcia, Max Naylor-Marlow, Paul R. Shearing, Mengzheng Ouyang, Lesley Cohen, Nigel P. Brandon and Billy Wu**

1. Materials

Lithium trifluoromethane-sulfonimide (LiTFSI) (purity >99% by NMR) was purchased from Sigma–Aldrich Co., Ltd. Manganese (II) acetyllacetonate ($Mn(AC)_2$) was obtained from Merck Schuchardt OHG in Germany. The PEDOT:PSS aqueous solution was purchased from Heraeus (Leverkusen, Germany). The weight ratio of PSS to PEDOT was 2.5.

2. The preparation of composite electrodes

Prior to deposition, the printed stainless steel scaffolds were washed by ethanol, acetone, and deionized water. Typically, the deposition was performed in the aqueous solution containing 50 ml (0.1 M) of manganese (II) acetyllacetonate ($Mn(AC)_2$) and 0.2 ml PEDOT:PSS aqueous solution (4 wt%) applying a DC voltage of 10.0 V. The as prepared electrode samples were dried at 80 °C for 12 h.

3. Pre-treatment and characterization

3.1 Pre-treatment of Scanning Electron Microscope (SEM) samples

The printed stainless steel scaffolds for SEM analysis was washed by ethanol, acetone, and deionized water, respectively. The prepared electrodes were washed in water after deposition. The SEM images of the printed scaffolds with/without deposition were characterized by scanning electron microscopy (JSM 5610 LV SEM, JEOL, Japan) at an acceleration voltage of 15 kV. The images with higher resolution were obtained using a ZEISS Auriga (Carl Zeiss Microscopy, Germany) at an acceleration voltage of 5 kV.

3.2 X-ray photoelectron spectroscopy (XPS) measurements

XPS Data Collection: The composite MnO_x-PEDOT:PSS was deposited directly onto the silver plate (5 mm x 5 mm) to overcome the existence of Mn from stainless steel. All XP spectrums were recorded using a K-alpha$^+$ XPS spectrometer equipped with a MXR3 Al Kα monochromated X-ray source (hν = 1486.6 eV). X-ray gun power was set to 72 W (6 mA and 12 kV). With this X-ray setting, the intensity of the Ag $3d_{5/2}$ photoemission peak for an atomically clean Ag sample, recorded at 20 eV pass energy (PE), was 5×10^6 counts s^{-1} and the full width at half maximum (FWHM) was 0.58 eV. Binding energy calibration was made using Au $4f_{7/2}$ (84.01 eV), Ag $3d_{5/2}$ (368.20 eV) and Cu $2p_{3/2}$ (932.55 eV). Charge compensation was achieved using the FG03 flood gun using a combination of low energy electrons and the ion flood source. Survey scans were acquired using 200 eV pass energy, 1 eV step size and 100 milliseconds (50 ms x 2 scans) dwell times. All high resolution spectra were acquired using 20 eV pass energy, 0.1 eV step size and 1 second (50ms x 20 scans = 1000 ms) dwell times. Samples were prepared by pressing the sample onto the sample holder with metal clips and analysed at an electron take-off angle normal to the surface with respect to the analyser.

XPS Data Analysis: Casa XPS was used for data interpretation. Shirley or two point linear background subtractions were employed depending on background shape. Thermo scientific sensitivity factors were used for quantification analysis. Peaks were fitted using GL(30) lineshapes; a combination of a Gaussian (70%) and Lorentzian (30%). In terms of charge correction, the main C 1s photoemission line was measured at 284.9 eV. The XPS spectra of the MnO_x-PEDOT:PSS composites were carried out to investigate the presence of MnO_x and PEDOT:PSS in the sample.

3.3 Zeta Potential measurement

PALS Zeta Potential Analyser version 3.48 (Brookhaven Instruments) was used to collect the Zeta potential of PEDOT:PSS in manganese aqueous solution. The results were obtained in a ×50 diluted solution at room temperature using the Smoluchowski model.

3.4 Raman measurements

The Raman system is a Renishaw RM-2000 confocal microscope CCD system. All measurements were carried out using the 514 nm laser focussed onto the surface through a × 50, short working distance, high numerical aperture microscope objective that resulted in a spot size of approximately 1.5 microns at the focal point. The incident laser intensity was optimised for each sample to ensure that there was no laser induced heating or damage and appropriate integration times were used for each measurement to ensure that a reasonable signal to noise ratio was achieved. The pure MnO_x electrode for Raman testing was prepared in a 0.1 M $Mn(AC)_2$ aqueous solution (80 mL) without addition of PEDOT:PSS. The MnOx-PEDOT:PSS electrodes were prepared in a 0.1 M $Mn(AC)_2$ aqueous solution with addition of PEDOT:PSS. All of the deposited electrodes were rinsed with deionized water to remove impurities and dried at 80 °C for 12 hours. The PEDOT:PSS solution was dried to obtain a thin film for Raman measurement.

3.4 X-ray tomography

The porous plate and array metallic scaffold (45-1200) with 15 min deposition of MnOx-PEDOT:PSS was studied. The high resolution scans were performed using the Zeiss Xradia Ultra 810, and the full body scans were performed using a Zeiss Xradia Versa 520. Both of the two "Versa" scans were performed using a primary voltage of 140 kV: before cycling (1601 projections with 5s exposure, 4x optical magnification and voxel size of 2.15 um) and after cycling (3201 projections with 4.5s exposure, 4x optical magnification and voxel size of 2.90 um). The Ultra scan consisted of 1551 projections with each image having an exposure time of 40 s, operating in absorption mode with a pseudo-monochromatic beam energy of 5.4 keV. The voxel size was 126.2 nm and the field of view was 65x65 um.

Reconstruction of the X-ray transmission images was conducted using a filtered back-projection reconstruction algorithm, yielding a .tiff image sequence which was analyzed using the Avizo Fire software package (FEI Co.). The Mn and steel phases were segmented in 3D, based on thresholding of grey values in the images, with artefacts from the scan removed and excluded from segmentation. The segmented images were then used to calculate surface area and volume of the two phases, with a cropped volume being used for this analysis. The edges of the cropped volume are excluded from the surface area calculation, and any internal pores of the steel phase that were not connected to the surface layer were filled in so that they did not erroneously contribute to the surface area of the steel. Is this way, only the 'top' surface of the steel and Mn phases was included in the calculations for a representative volume of the electrode (the bottom, end and side faces of the cropped volume are 'capped' and excluded), and the values are not artificially inflated.

Geometric area of the cropped volume used for analysis was 2581x2265 µm = 5825218 μm^2. Steel area: precycle = 47590384 μm^2, post cycle = 40131724 μm^2. Mn area: precycle = 75643776 μm^2, post cycle = 50863352 μm^2. SA ratios (actual SA/geometric SA): Steel precycle = 8.17, post cycle = 6.89, Mn precycle = 12.99, post cycle = 8.73.

4. Electrochemical Measurements

The pseudocapacitors were tested using a typical three-electrode configuration in LiTFSI aqueous electrolyte (0.25 M). The as-prepared samples were used as the working electrodes with an electrode area of 0.25 cm^2, the platinum plate electrode was used as counter electrode, and a saturated calomel electrode (SCE) was used as reference electrodes. The electrochemical properties of the MnO_x-PEDOT:PSS deposited electrodes were tested on a Metrohm Autolab PGSTA302N potentiostat-galvanostat (The Netherlands). To measure the mass of the deposition, all of the scaffolds and electrodes were dried at 80 °C for 12 hours to remove absorbed water.

5. Figures

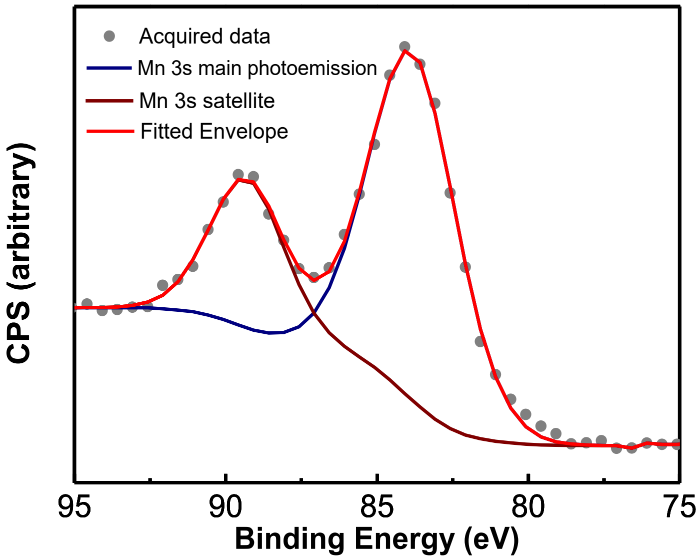

Figure S1. Mn 3s high resolution XPS spectrum of MnO_x-PEDOT:PSS.

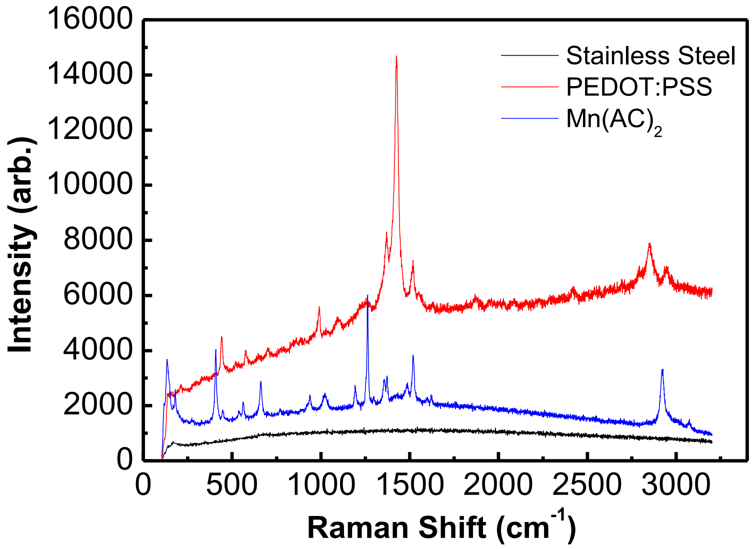

Figure S2. Raman spectra of the stainless steel, PEDOT:PSS, and $Mn(AC)_2$.

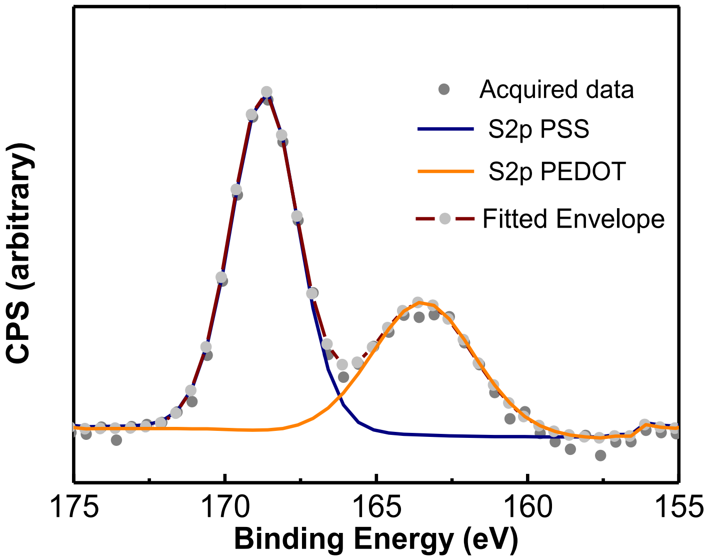

Figure S3. S 2p high resolution XPS spectrum of MnO_x-PEDOT:PSS.

Table S1. Relative atomic percentages:

Oxygen	Carbon	Manganese	Sulphur
42.5	40.4	13.7	3.4

Figure S4. Photograph of 3D-printed stainless steel scaffolds fabricated using various laser power and scan rates.

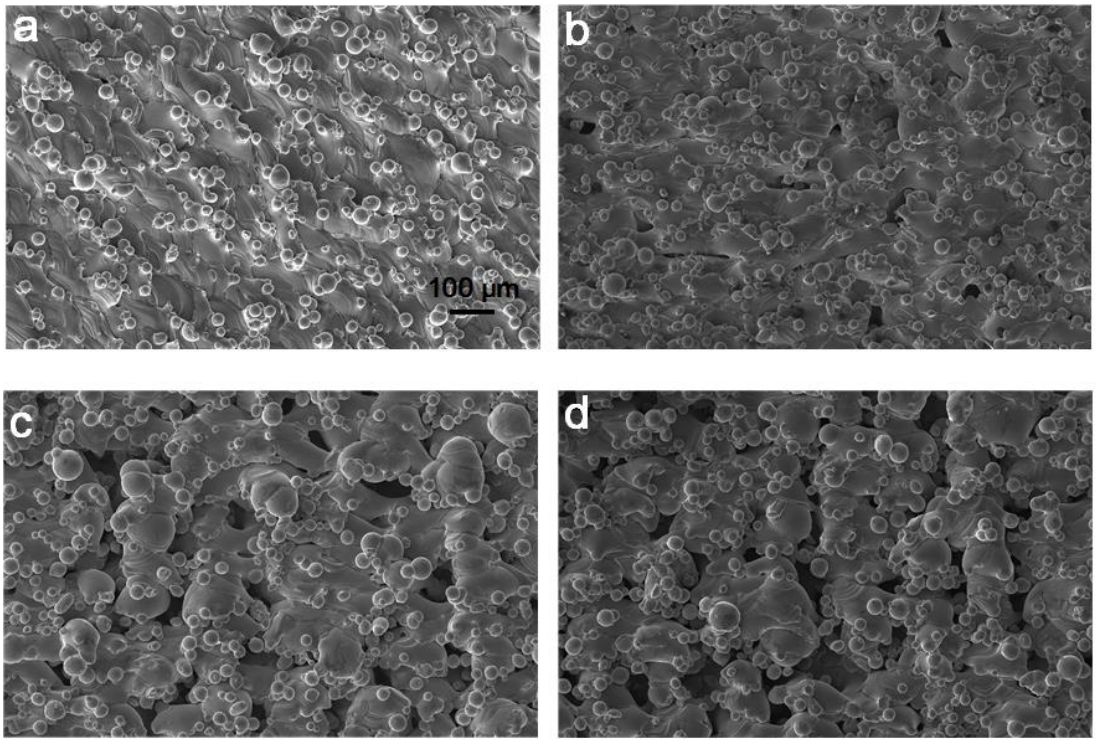

Figure S5. SEM images of the printed stainless steel plates fabricated using various laser parameters: (a) 45-600 (a laser power of 45 W and scan speed of 600 mm/s, 45-600 is used here to represent the laser power (W) and scan speed (mm/s) respectively), (b) 45-900, (c) 45-1200 and (d) 45-1500.

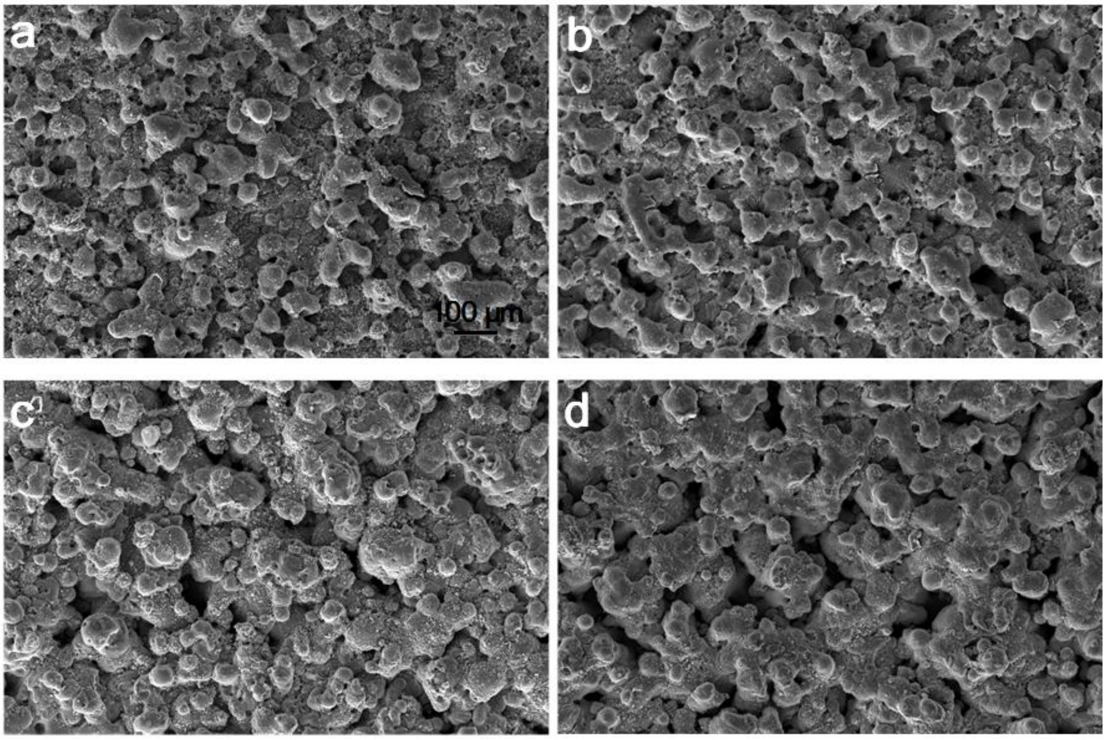

Figure S6. SEM images of the printed stainless steel plates fabricated using various laser parameters with 15 min deposition of MnO_x-PEDOT:PSS: (a) 45-600, (b) 45-900, (c) 45-1200 and (d) 45-1500.

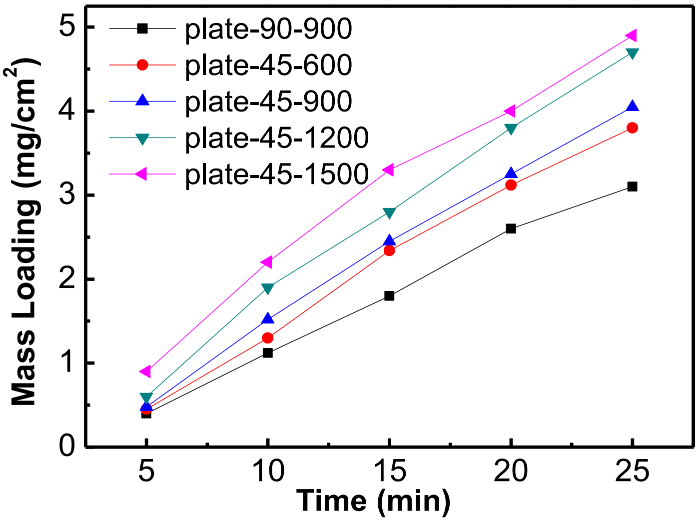

Figure S7. The mass loading of the deposited MnO_x-PEDOT:PSS on printed plates as a function of deposition time, for various laser parameters.

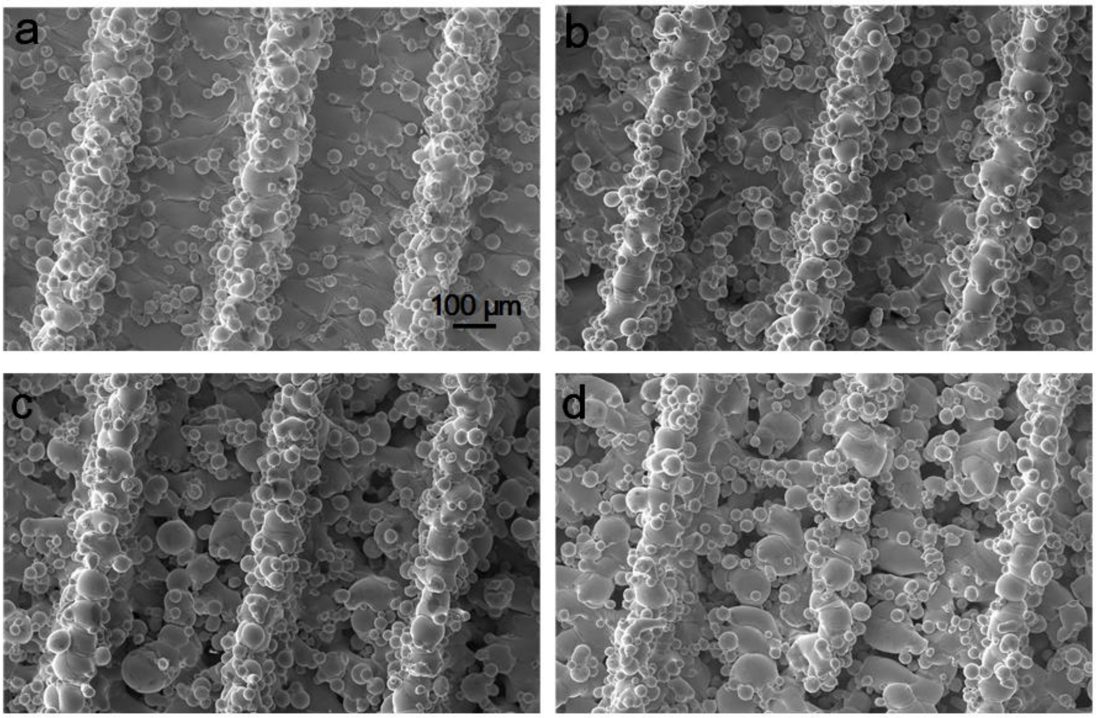

Figure S8. SEM images of the printed stainless steel plate and arrays fabricated using various laser parameters: (a) 90-1500, (b) 45-600, (c) 45-900, and (d) 45-1500.

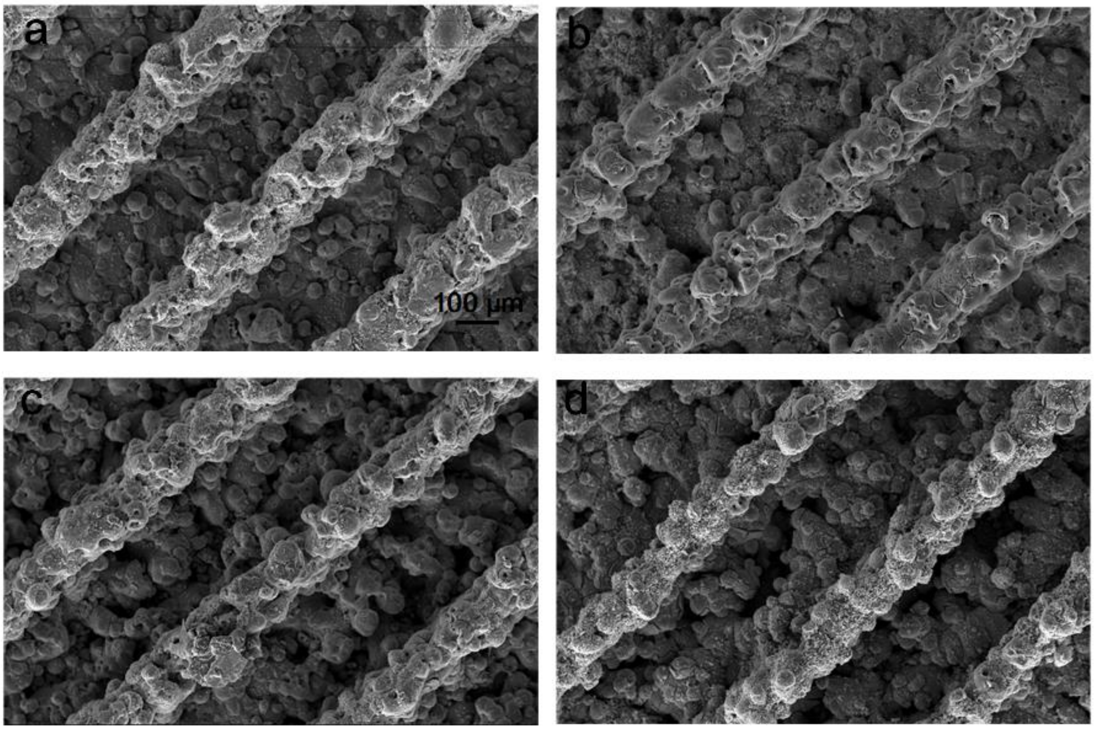

Figure S9. SEM images of the printed stainless steel plate and arrays fabricated using various laser parameters with 15 min deposition of MnO_x-PEDOT:PSS: (a) 90-1500, (b) 45-600, (c) 45-900, and (d) 45-1500.

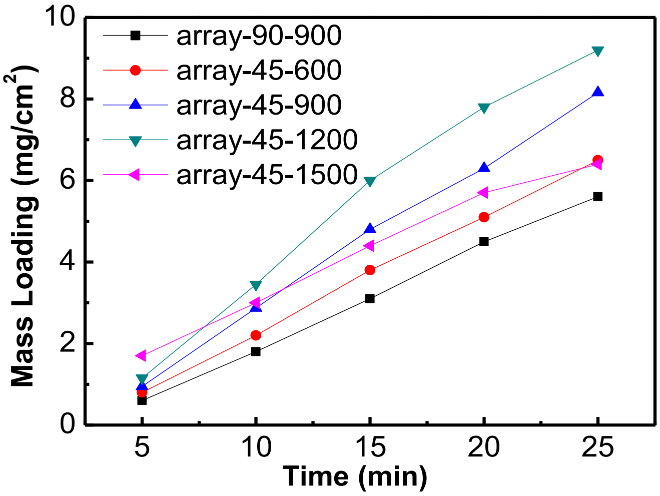

Figure S10. The mass loading of the deposited MnO_x-PEDOT:PSS on printed plate and as a function of deposition time, for various laser parameters.

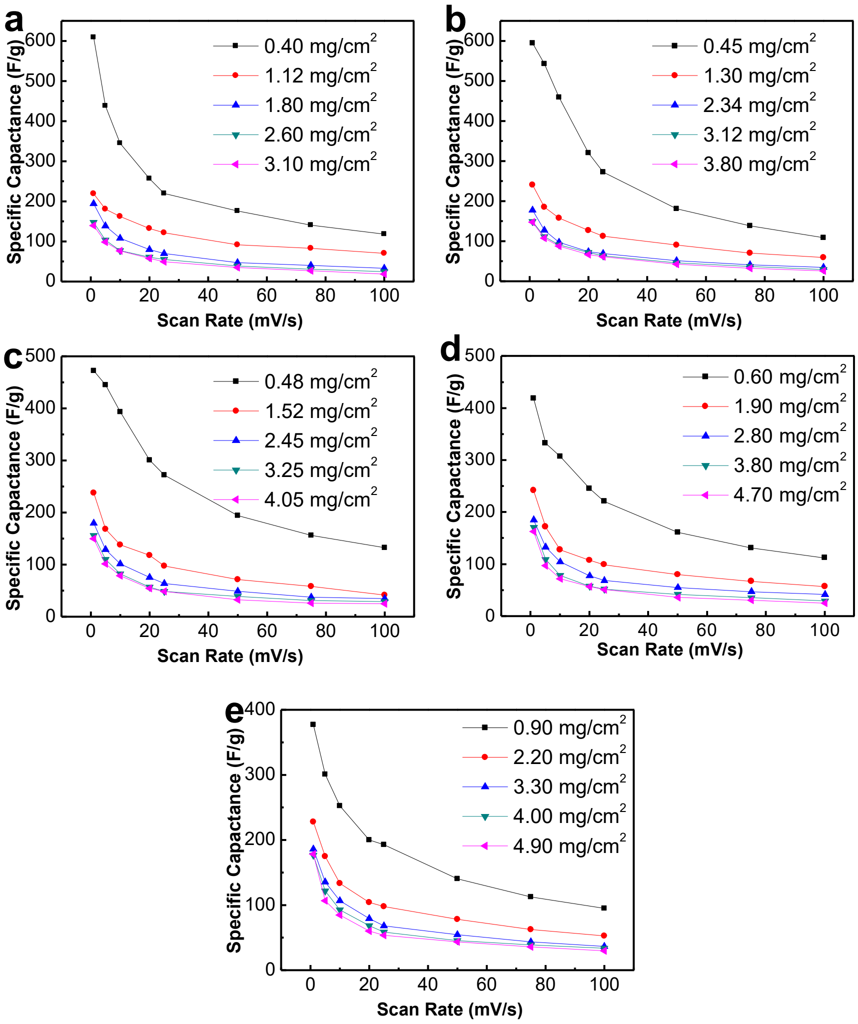

Figure S11. The specific capacitance *vs* scan rate of the printed scaffolds with different print laser parameters: a) 90-1500, b) 45-600, c) 45-900, d) 45-1200, and e) 45-1500 and various mass loading of MnO_x-PEDOT:PSS.

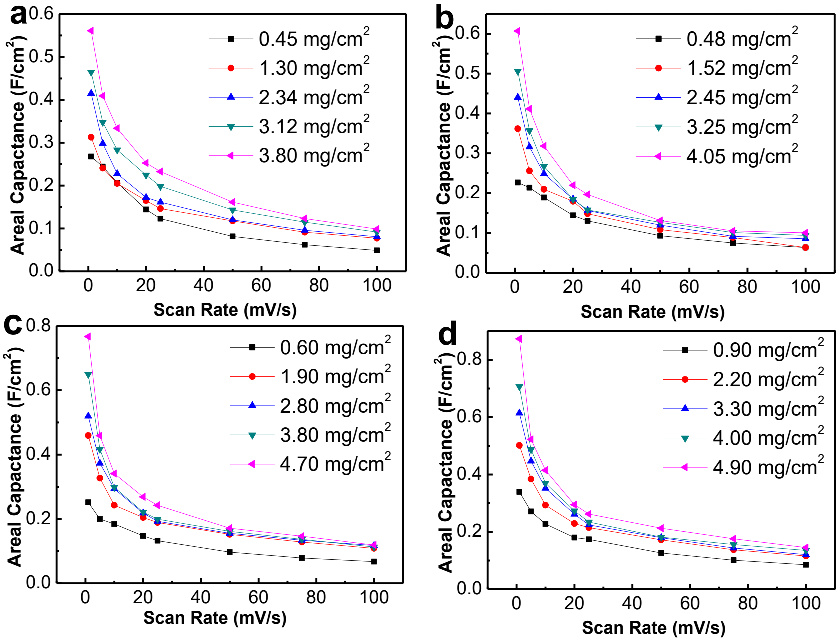

Figure S12. The areal capacitances vs scan rate of MnO_x-PEDOT:PSS on the surface of printed plates with various mass loadings applying different printing laser parameters: a) 45-600, b) 45-900, c) 45-1200, and d) 45-1500.

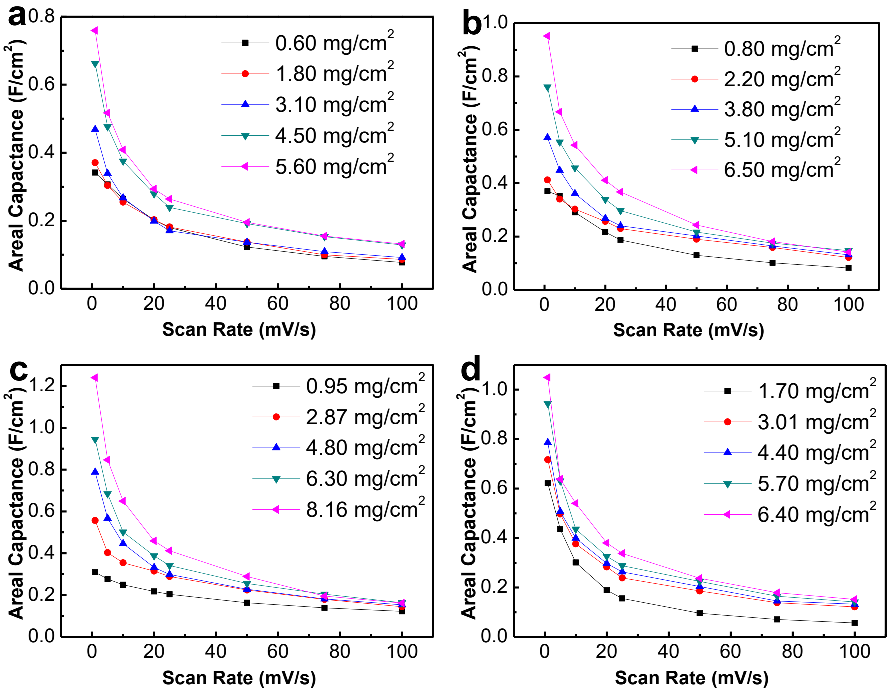

Figure S13. The areal capacitances vs scan rate of MnO_x-PEDOT:PSS on the surface of printed plate and array scaffolds with various mass loadings applying different printing laser parameters: a) 90-1500, b) 45-600, c) 45-900, and d) 45-1500.

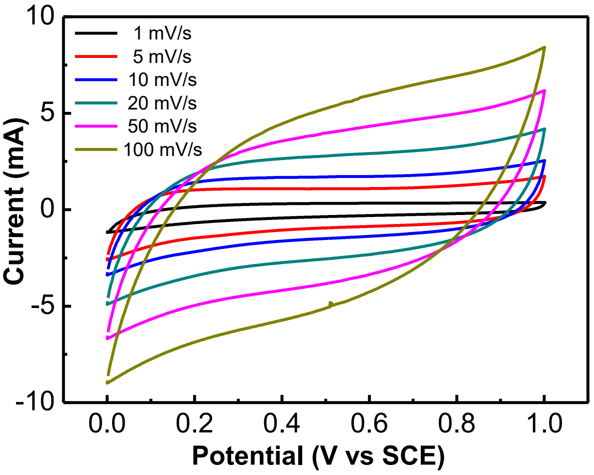

Figure S14. CV curves of porous plate and array (45-1200) with 25 min deposition of MnO_x-PEDOT:PSS at different scan rates.

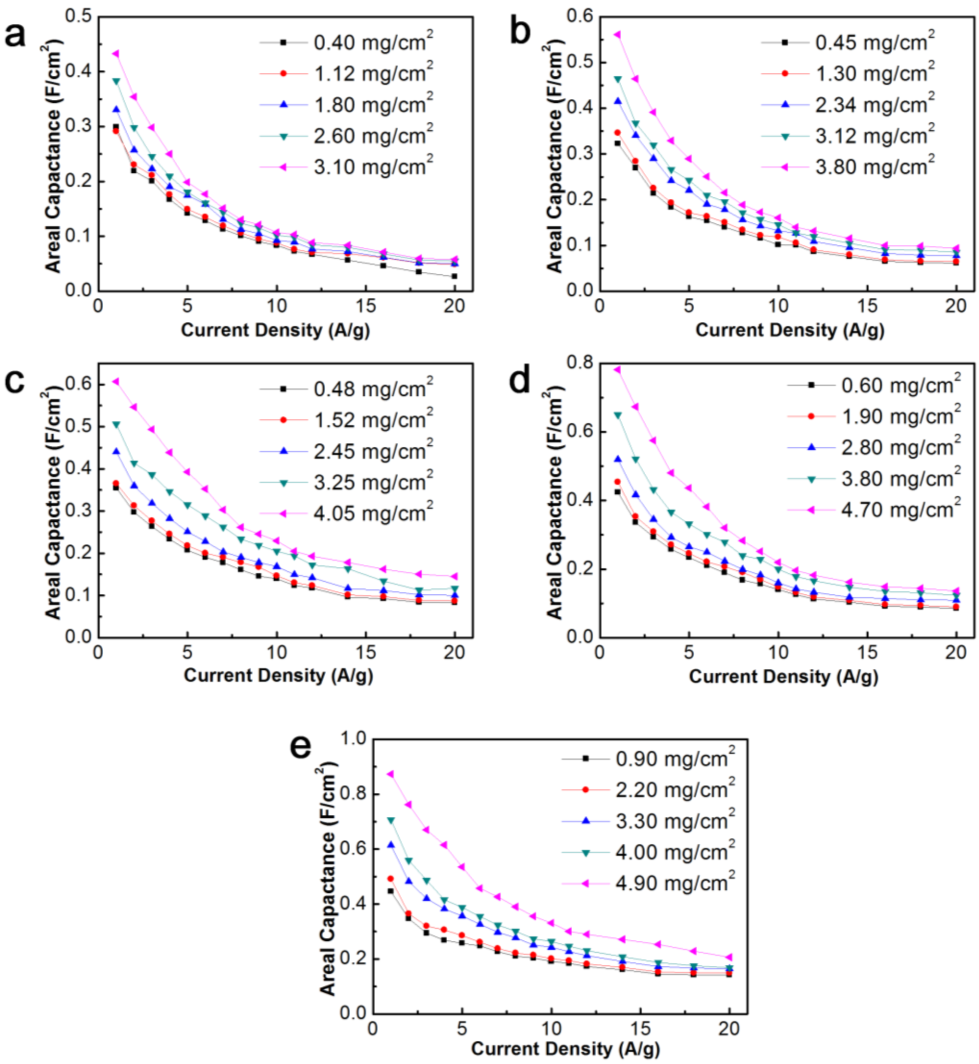

Figure S15. The areal capacitances vs current density of MnO_x-PEDOT:PSS on the surface of printed plate and array scaffolds with various mass loadings applying different printing laser parameters: a) 90-1500, b) 45-600, c) 45-900, d) 45-1200, and e) 45-1500.

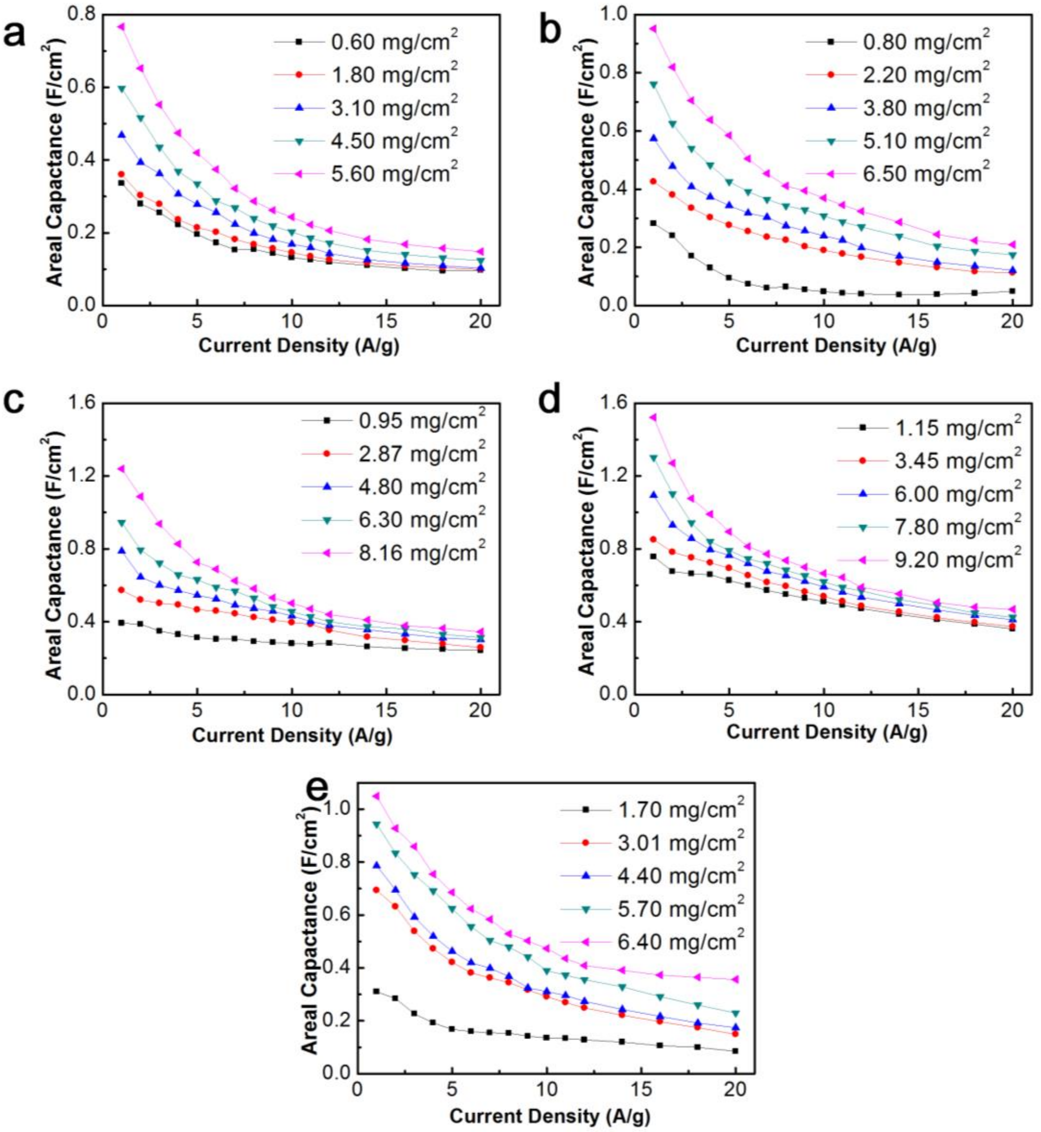

Figure S16. The areal capacitances vs current density of MnO_x-PEDOT:PSS on the surface of printed plate and array scaffolds with various mass loadings applying different printing laser parameters: a) 90-1500, b) 45-600, c) 45-900, d) 45-1200, and e) 45-1500.